6-6-2022

Probing the Link between Pancratistatin and Mitochondrial Apoptosis through Changes in the Membrane Dynamics on the Nanoscale

Stuart R. Castillo
University of Windsor

Brett W. Rickeard
University of Windsor

Mitchell Dipasquale
University of Windsor

Michael H.L. Nguyen
University of Windsor

Aislyn Lewis-Laurent
University of Windsor

Probing the link between Pancratistatin and mitochondrial apoptosis through changes in the membrane dynamics on the nanoscale

Stuart R. Castillo,[†,‡] Brett W. Rickeard,[†,‡] Mitchell DiPasquale,[†] Michael H. L. Nguyen,[†] Aislyn Lewis-Laurent,[†] Milka Doktorova,[¶] Batuhan Kav,[§,‖] Markus S. Miettinen,[§] Michihiro Nagao,[⊥,#,@] Elizabeth G. Kelley,[⊥] and Drew Marquardt[*,†,△]

†*University of Windsor, Department Chemistry and Biochemistry, Windsor, N9B 3P4, Canada*

‡*these authors contributed equally to this work*

¶*University of Virginia School of Medicine, Department of Molecular Physiology and Biological Physics, Charlottesville, 22903, USA*

§*Max-Planck Institute of Colloids and Interfaces, Potsdam,14476, Germany*

‖*Institute of Biological Information Processing: Structural Biochemistry (IBI-7), Forschungszentrum, Julich, 52428 Julich, Germany*

⊥*National Institute of Standards and Technology, Center for Neutron Research, Gaithersburg, 20899, USA*

#*University of Maryland, Department of Materials Science and Engineering, College Park, 20742, USA*

@*University of Delaware, Department of Physics and Astronomy, Newark, 19716, USA*

△*University of Windsor, Department of Physics, Windsor, N9B 3P4, Canada*

E-mail: drew.marquardt@uwindsor.ca

Abstract

Pancratistatin (PST) is a natural antiviral alkaloid that has demonstrated specificity towards cancerous cells and explicitly targets the mitochondria. PST initiates apoptosis while leaving healthy, noncancerous cells unscathed. However, the manner by which PST induces apoptosis remains elusive and impedes the advancement of PST as a natural anticancer therapeutic agent. Herein, we use neutron spin-echo (NSE) spectroscopy, molecular dynamics (MD) simulations, and supporting small angle scattering techniques to study PST's effect on membrane dynamics using biologically representative model membranes. Our data suggests that PST stiffens the inner mitochondrial membrane (IMM) by preferentially associating with cardiolipin, which would lead to the relocation and release of cytochrome *c*. Secondly, PST has an ordering effect on the lipids and disrupts their distribution within the IMM, which would interfere with the maintenance and functionality of the active forms of proteins in the electron transport chain. These previously unreported findings implicate PST's effect on mitochondrial apoptosis.

Keywords

Cancer, Lipid membranes, Vesicles, Anti-cancer drugs, Apoptosis, Natural compounds, Nanomedicine, Neutron Spin-Echo, Small angle x-ray scattering, Small angle neutron scattering, Molecular dynamics

Introduction

Conventional cancer treatments use highly cytotoxic agents in combination with radiation therapy that act on both cancerous and noncanerous cells eliminating or reducing tumor growth. Unfortunately, these traditional methods and drugs (e.g., DNA intercalating agents) are genotoxic and have the potential to lead to the manifestation of additional cancers

later in life.[1] Recently, focus has shifted towards a more targeted drug therapy approach; one that displays little to no toxic effects towards healthy cells. In particular, mitocans that specifically target the mitochondria of cancerous cells and induce apoptosis can be utilized.[2] By exploiting this process to target and eliminate cancerous cells, natural antiviral alkaloids such as Pancratistatin (PST) emanating from the *Amaryllidaceae* family can be used to induce apoptosis (Fig 2C).[3] PST was first extracted from the Hawaiian roots of *Pancratium littorale*, more commonly known as the *spider lilly*,[4] and has successfully shown anticancer activity in multiple human cancer cell lines including: breast, liver, pancreatic, testicular, and neuroblastoma cancer cells.[3,5] Natural derivatives from the Amaryllidaceae family of plants have not only yielded anti-cancer compounds such as PST,[6] Narciclasine[7] and Haemanthamine,[8] but also compounds with anticholinesterase, antimalarial, antiviral, and anti-inflammatory properties.[9,10] Regardless of PST's effectiveness towards targeting and treating cancer, two significant concerns must be addressed. First, the low availability of PST coupled with the costly and time-consuming synthesis of synthetic PST has vastly diminished the progress of research. Second, the biochemical mechanism of action by which PST selectively targets and induces mitochondrial apoptosis within cancerous cells is still unclear.[3] More recently, work has shown that PST treatment leads to phosphatidylserine leaflet scrambling, caspase-3 activation, generation of reactive oxygen species (ROS), and loss of mitochondrial membrane potential.[11,12] While these findings are key to understanding PST's function and effect within the mitochondria, they do not offer the exact nature of how PST operates and selects for cancerous cells to initiate mitochondrial apoptosis.

There are two distinct signalling pathways that lead to apoptosis in mammalian cells. First, through the extrinsic receptor-mediated pathway initiated by death receptors in the plasma membrane, and second, via the intrinsic mitochondria-mediated pathway initiated by the disruption of intracellular homeostasis.[13,14] The present study is interested in the latter and how PST may initiate this pathway. The role of cytochrome *c*, a heme containing protein, has been thoroughly investigated with respect to apoptosis. It has been shown to

play a critical role upon release into the cytoplasm, triggering caspase activation and eventual cell death.[15–18] The localization of cytochrome c, within the inner mitochondrial membrane (IMM), is of great interest as it is only found in the free cytosolic form within the IMM matrix or bound to cardiolipin (CL) —a phospholipid virtually exclusive to the IMM.[19,20] However, the peroxidation of CL leads to the detachment of cytochrome c and subsequently its release into the cytosol, initiating the apoptotic cascade.[21] Additionally, the localization of CL bound cytochrome c can drive the peroxidation of CL, aiding in the release of cytochrome c into the cytoplasm via the pores of the outer mitochondrial membrane.[21,22] Although the role of CL in mitochondrial apoptosis has been previously investigated, to our knowledge the investigation of PST, and its role on bilayer mechanical properties, such as membrane fluidity and rigidity, and how changes in these properties may trigger mitochondrial apoptosis are severely under researched. To this end, we employed an array of scattering techniques to investigate PST's effect on membrane structure and dynamics, correlating such effects to its biological activity.[23,24]

Here, the effect of PST on the mechanical properties of a mitochondrial membrane mimic was investigated using neutron spin-echo (NSE). NSE has been previously used to investigate change in the effective bending modulus $\widetilde{\kappa}$, in biomimetic membranes with respect to acyl chain length, varying temperature, ionic liquids, and electronic-cigarette/vaping additives such as vitamin E acetate (VEA).[25–27] NSE is uniquely suited to measuring the thermally-induced membrane undulations at the nanometer and nanosecond length- and time-scales, respectively, for the direct measurement of the effective bending modulus $\widetilde{\kappa}$, thereby quantifying membrane rigidity which ultimately controls membrane fluctuations on the length scales of the membrane itself. Alteration in membrane rigidity influences the interactions and insertion of membrane proteins,[28] size and morphology of lipid rafts,[29] and drug-membrane interactions.[30] These nanoscale fluctuations play a critical role in maintaining the IMM and allowing CL to act as a proton trap and protein stabilizing agent, as well as allowing for the functionality of active protein forms in the electron transport chain (ETC).[31] CL has also

been shown to form microdomains in the IMM and act as a platform for apoptotic signals facilitating apoptotic execution.[32] Therefore, alteration in membrane fluctuations by PST could lead to enhanced apoptotic activity in the mitochondria and can provide an understanding of PST's biochemical mechanism of action. The present study combines the use of neutron, X-ray and light scattering techniques in combination with molecular dynamics simulations to investigate the never before reported mechanical and structural effects of PST on an IMM-mimic.

Methods

Materials

1',3'-bis[1,2-dioleoyl-*sn*-glycero-3-phospho]-glycerol (sodium salt) [18:1 Cardiolipin], 1-palmitoyl-2-oleoyl-glycero-3-phosphocholine [16:0/18:1 PC, POPC], 1-palmitoyl-2-oleoyl-*sn*-glycero-3-phosphoethanolamine [16:0/18.1 PE, POPE] were purchased from Avanti Polar Lipids (Alabaster, AL) and were used as received. Lipids were prepared as stock solutions in HPLC-grade chloroform (Sigma-Aldrich, Oakville, ON). Dimethyl sulfoxide-d6 (DMSO-d6) and D_2O (99.9%) were purchased from Cambridge Isotopes (Andover, MA). Pancratistatin (PST) was purchased from Toronto Research Chemicals (North York, ON).

Preparation and Characterization of Vesicles

Lipid films were prepared by transferring the desired volumes of stock lipid solutions to separate glass scintillation vials to create the desired composition for the IMM: TOCL/POPE/POPC (0.25/0.25/0.50), TOCL/POPE (0.50/0.50), or TOCL/POPC (0.50/0.50). Bulk organic solvent was removed under a gentle stream of argon, and the resulting lipid films were dried overnight ($\approx$ 12 h) under vacuum at room temperature. Films were hydrated to a concentration of 25 mg/mL with D_2O warmed at 50 °C, and the resulting multilamellar vesicles (MLVs) were subjected to 5 freeze/thaw cycles (-80 °C and 50 °C) with intermittent vortex-

ing. To create unilamellar vesicles, the MLVs were extruded by passing the samples through a hand-held mini extruder equipped with a 100 nm pore-diameter polycarbonate filter (Avanti Polar Lipids, Alabaster, AL) 31 times. Extrusion was done at a temperature of 45 °C, above the lipids' melting transition temperature. The extruded LUVs were characterized by dynamic light scattering (DLS) using a Malvern ZetaSizer Nano ZS (Malvern Panalytical, Ltd., Malvern, UK) equipped with a He - Ne laser (λ = 633nm). For DLS measurements, large unilamellar vesicles suspended in D_2O were diluted to a concentration of 1 mg/mL and measured at a temperature of 37 °C with a fixed scattering angle of 175°. With DLS, information regarding diffusion of molecules from fluctuations in light intensity is used to determine the diffusion coefficient and the hydrodynamic radius. DLS measures the time-dependant fluctuations in the scattered light, where the rate of fluctuations is related to the diffusion of a molecule through the solvent.

PST was prepared as a DMSO-d6 stock at a concentration of 9.5 mg/mL and was added to select samples at mole fractions of 0.01, 0.015, and 0.02 of total lipid. This concentration led to the total amount of DMSO-d6 to be less than 2 mole percent present in solution. To confirm no aggregates were formed in solution, an aggregation index was extracted using DLS and resulted in a value of -0.0960, indicating there was no PST aggregates. PST was incubated with the extruded LUV samples for 12 h at 37 °C before any experimental analysis was conducted.

Small-Angle Neutron and X-Ray Scattering

SANS measurements were conducted on the NGB 30 m SANS instrument located at the National Institute of Standards and Technology Center for Neutron Research (NCNR, Gaithersburg, MD).[33] A wavelength of 6 Å was used with two sample-to-detector distances (1 m and 4 m) to access a scattering vector range of approximately 0.01 $Å^{-1} < Q < 0.5$ $Å^{-1}$. LUVs were diluted down to a concentration of 10 mg/mL in D_2O, loaded into 1 mm path-length quartz banjo cells (Hellma USA, Plainsview, NY) and mounted in a Peltier temperature-controlled

cell holder with ≈ 1 °C accuracy. The scattered beam was counted on a 2D ^{3}He detector and subsequently corrected for detector pixel sensitivity, dark current, sample transmission, and background scattering from D_2O, radially averaged, and stitched using Igor Pro and the NCNR developed reduction scripts.[34] SANS data were analyzed using Vesicle Viewer software.[35] Small angle X-ray scattering (SAXS) experiments were carried using the 12-ID-B beamline at the Advanced Photon Source (Argonne National Laboratory, Lemont, IL). An average photon energy of 13.3 keV was used, and data were collected using a 2M Pilatus detector (Dectris Ltd., Philadelphia, PA) set at a sample-distance of 2.0106 m. X-rays with a wavelength of 0.9322 Å were used. The resulting form factors in the scattering vector range of 0.03 $Å^{-1}$ < Q < 0.9 $Å^{-1}$ were background corrected using the established on-site reduction workflow and analyzed using Vesicle Viewer software.[35] All measurements were collected at 37 °C. LUVs at a concentration of 15 mg/mL in H_2O were loaded into temperature controlled capillary-flow cells. These fluid filled capillaries oscillated ≈ 100 μL of sample to avoid ionization damage. Samples were measured for 45 frames, with 0.5 second exposure and 1.5 second rest, also to avoid damage.

Neutron Spin-Echo Spectroscopy and Data Treatment

Data were collected on the NG-A NSE spectrometer at the NCNR. Neutron wavelengths of 8 Å and 11 Å were used to obtain a scattering vector range of 0.04 $Å^{-1}$ < Q < 0.11 $Å^{-1}$ with Fourier times of up to 100 ns. These settings allow measurement of bilayer motions on length scales of ≈ 5 nm to 20 nm and time scales of 0.1 ns to 100 ns. LUVs at a concentration of 10 mg/mL in D_2O were loaded into cells with a 4 mm path length for NSE measurements. All samples were measured at 37 °C. Samples were equilibrated at the desired temperatures for 30 minutes prior to evaluation; the temperature was maintained within ≈ 1 °C. The resulting NSE data was reduced using the Data Analysis and Visualization Environment software package (DAVE).[36]

For any given Q value obtained from NSE, the resulting measurement is the intermediate

scattering function, $I(Q,\tau)/I(Q,0)$. By using the Zilman and Granek model collectively with Hoffmann's model to account for large diffusing particles (vesicles), the decay rate Γ_{ZG} is defined as:

$$\frac{I(Q,\tau)}{I(Q,0)} \simeq e^{-DQ^2t} e^{-(\Gamma_{ZG}t)^{2/3}} \tag{1}$$

where D is the Stokes-Einstein diffusion coefficient $D = \frac{\kappa_B T}{6\pi\eta R}$ and is dependant on the hydrodynamic radius of the vesicle R, solvent viscosity η, absolute temperature T, and κ_B as the Boltzmann constant. In this study, D was measured by dynamic light scattering (DLS).

The work done by Zilman and Granek was extended by Watson and Brown to account for a structure with finite thickness and internal dissipation within the bilayer which cannot be accurately described by a thin structure-less sheet.[37,38] Their work showed that the effective bending modulus, $\widetilde{\kappa}$, measured by NSE is related to the intrinsic bending modulus κ through:

$$\widetilde{\kappa} = \kappa + 2d^2 k_m \tag{2}$$

where d is the distance of the neutral surface from the bilayer midplane and k_m is the monolayer compressibility modulus.[37] By combining both theories and assuming that the neutral surface is located at the hydrophobic-hydrophilic interface, we are able to obtain κ from the plot Γ_{ZG} versus Q^3 from:[39]

$$\Gamma_{ZG} = 0.0069\sqrt{\frac{\kappa_B T}{\kappa}}\frac{\kappa_B T}{\eta} Q^3 \tag{3}$$

Molecular Dynamics Simulations

Atomistic MD simulations were performed using the GROMACS 2018.3 package and the CHARMM36 force fields.[40,41] The CHARMM PST force field was generated by the CGenFF[42,43] version 4.0 with the CHARMM36 force field version Nov-2018. Prior to the production runs for the PST containing membranes, multiple small simulation runs (20 ns each) were exe-

cuted to bring the PST molecules closer to the membrane. All membrane compositions were generated using the CHARMM-GUI input generator.[44] The composition of all simulated systems and their total simulation times can be seen in Table 1

Table 1: Lipid compositions used for MD simulations, including the duration of the simulation. Each composition contains lipid, water, sodium, and PST.

Composition	Simulation Time (ns)	Number of Molecules					
		TOCL	POPC	POPE	H_2O	Na^+	PST
IMM Mimic	570	30	60	30	9000	60	0
IMM Mimic w/ 1.0% PST	560	30	60	30	8987	60	1
IMM Mimic w/ 1.5% PST	570	30	60	30	8971	60	2
IMM Mimic w/ 2.0% PST	550	30	60	30	8955	60	3
TOCL/POPC Control	540	60	60	0	12000	120	0
TOCL/POPC w/ 1.0% PST	530	60	60	0	11984	120	1
TOCL/POPC w/ 2.0% PST	550	60	60	0	11955	120	3
TOCL/POPE Control	530	60	0	60	12000	120	0
TOCL/POPE w/ 1.0% PST	560	60	0	60	11982	120	1
TOCL/POPE w/ 2.0% PST	560	60	0	60	11957	120	3
TOCL Control	560	90	0	0	13500	180	0

Energy minimization and equilibration steps were performed according to the CHARMM-GUI guidelines. The energy minimization began with steepest-descent minimization for 5000 steps followed by ensemble equilibration for 50 ps with a timestep of 1 fs, followed by isothermal-isobaric ensemble equilibration for 325 ps at a timestep of 2 fs, with semi-isotropic pressure coupling accomplished using the Berendsen barostat.[45] Equilibration was monitored by observing the area per lipid of the system.

Unconstrained MD simulations were run for over 500 ns for each composition using a timestep of 2 fs. All simulations were kept at 37 °C using velocity-rescaling temperature coupling.[46] Pressure coupling was applied using the Parrinello-Rahman barostat.[47] A zero surface tension ensemble was created by setting a reference pressure of 1 bar for both the bilayer plane and the normal to the bilayer. Bilayer compressibility was set to 0.000045 bar^{-1} as previously measured via neutron diffraction.[48] Van der Waals interactions were cut off at 1.2 nm, and the interactions were modified using the force-switch method between 1.0 nm - 1.2 nm. Long-range electrostatics were determined using the particle mesh Ewald

method with a cutoff of 1.2 nm.[49] The final 500 ns of the unrestrained MD simulations was used for data analysis. A combination of in-house scripts, GROMACS tools, and the Visual Molecular Dynamics (VMD) 1.9 program were used to analyze the simulations.[50] All errors were estimated using cumulative averaging.

The bending moduli of the simulated bilayers were calculated from the trajectories by analyzing the fluctuations in splay angles between pairs of neighboring lipids as described previously.[51] Briefly, the orientation of each lipid was defined by a vector connecting the center of mass of its glycerol backbone region with the center of mass of the last 3 atoms on the lipid's acyl chains. The splay angle between any two lipids that are near neighbors, i.e. whose centers of mass are within a cutoff distance of 14 Å, was then calculated as the angle between the lipids' director vectors. The probability distribution of the splay angles for any pair of lipids (e.g. POPC-POPC, POPC-TOCL, POPE-TOCL) was used to obtain the splay modulus for that lipid pair. The splay moduli of all lipid pairs in the system were then averaged to obtain the bending modulus of the bilayer. For a detailed description of the theoretical framework and its implementation see.[51–53]

We used MD simulations to assess PST-induced changes to the lateral (in-plane) diffusion of lipid species in the IMM-mimic membrane, see Table S2.

First, the mean squared displacement (MSD) $\langle r^2(t) \rangle$, i.e., the average of the square of the lateral displacement r of the center of mass of a tracer lipid during a time period t, was calculated for each lipid species. Here the angular brackets $\langle \cdot \rangle$ indicate average over all the periods of length t during the whole (500 ns) analysis period and over all the tracer lipids that were tracked in the analysis. The displacements were calculated in the center-of-mass coordinate system of the IMM-mimic membrane.

In practice, the Gromacs version 2018.3 tool `gmx traj` with the `-nojump` and `-com` switches was used to create the tracer lipid center of mass trajectories, and the tool `gmx msd` with the `-lateral z` and `-rmcomm` switches to calculate the MSDs.

From the slope of the fit to the linear region (50 to 150 ns) of the MSDs, the lateral

diffusion coefficient D was obtained directly by using its definition

$$D = \lim_{t\to\infty} \frac{1}{4t} \left\langle r^2(t) \right\rangle . \tag{4}$$

To estimate the error in D, the lipid populations were divided into five equally-sized groups, which were treated as independent measurements of the MSDs, thus providing the standard errors of the mean as a function of t, see Figure. S1 (the shaded regions). The error estimates for D were then obtained from the maximal and minimal slopes that fit within these error estimates for MSD in the fitting range (50 to 150 ns).

Results

Pancratistatin's Effect on Membrane Rigidity

To investigate PST effects on bilayer mechanics, we used an IMM mimic based on the major lipid species present in eukaryotic mitochondria cells as follows: tetraoleoyl cardiolipin (TOCL), palmitoyl-oleoyl phosphocholine (POPC), and palmitoyl-oleoyl phosphoethanolamine (POPE) at a mole fraction (χ) of 0.25/0.50/0.25.[54] Three additional compositions were used throughout the study: TOCL/POPC, TOCL/POPE, and TOCL at mole fractions (χ) of 0.50/0.50, 0.50/0.50, and 1, respectively. These compositions were used to monitor the behaviour of TOCL in the presence or absence of POPE and POPC and further investigate the role of TOCL in determining the structure and dynamics of mitochondrial membranes. With CL being the primary lipid of interest, the rationale for using TOCL rather than other CL compositions was due to the abundance of 16:0-18:1 hydrocarbon tails in the IMM.[55,56] From here forth CL will be used interchangeably with TOCL.

NSE spectroscopy offers unmatched capabilities in regards to measuring the collective dynamic properties of membranes on the length- and time-scale of local bilayer undulations (Figure 1, top). The IMM mimic as well as the other compositions were measured at 37

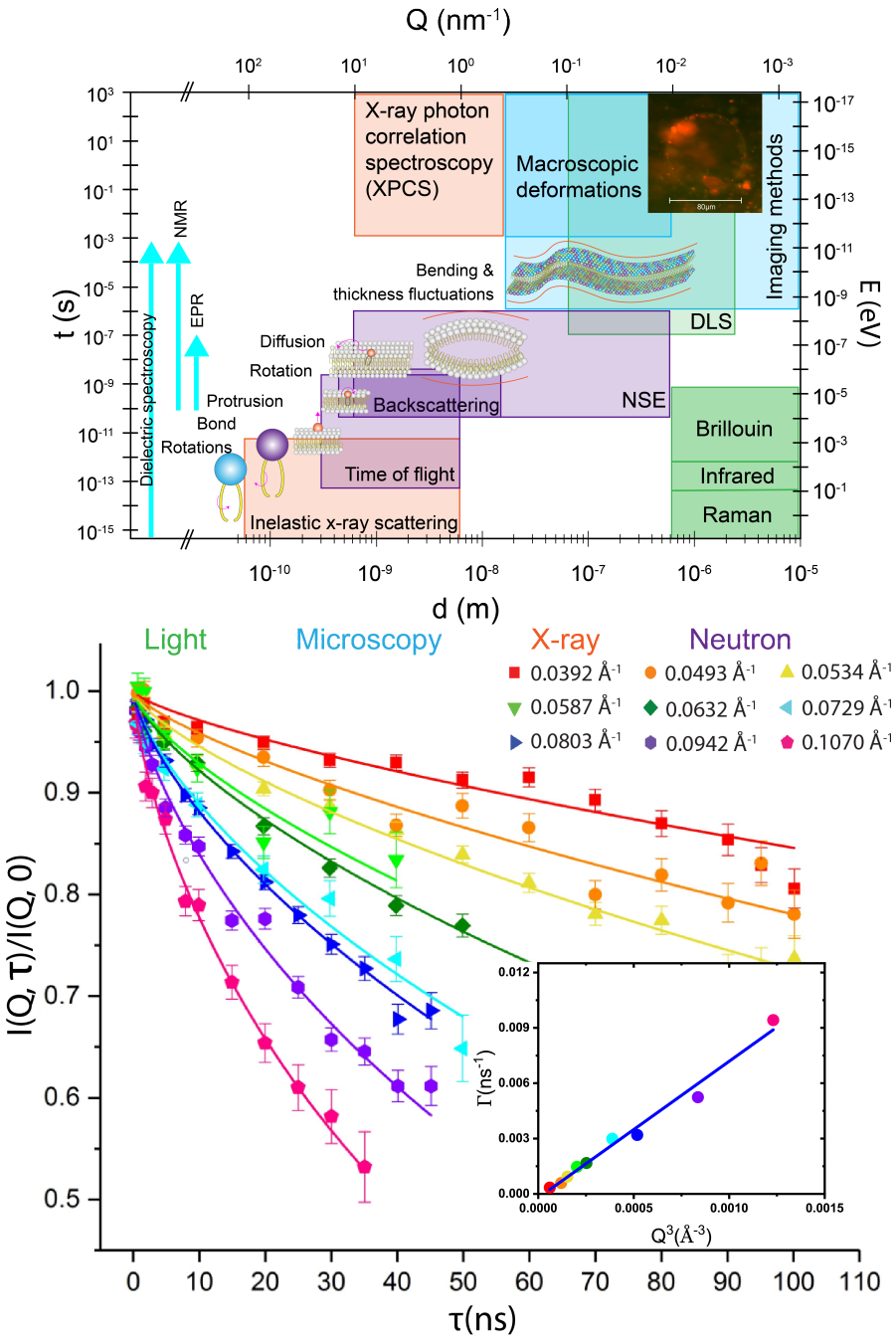

Figure 1: Top: Exhibiting the time (t) and length scales (d) as well as the corresponding energy (E) and momentum transfer (Q) accessible by various spectroscopic techniques. Figure adapted from ref.[57] Bottom: Normalized intermediate scattering function $I(Q,\tau)/I(Q,0)$ for various Q indicated by different colours for the IMM-mimic LUVs in D_2O at 37 °C, measured by NSE. The inset shows the linear dependence of the relaxation rate (Γ_{ZG}) with respect to Q^3. Error bars represent one standard deviation here and throughout the manuscript.

°C at varying concentrations of PST (mole fractions of 0.01, 0.015, and 0.02) (Table S5). The normalized intermediate scattering function, $I(Q,\tau)/I(Q,0)$ was measured over a range of Q-values corresponding to length scales greater than the bilayer thickness but less than the vesicle radii and Fourier times, τ, up to 100 ns. The data measured for the IMM at 37 °C is seen in Fig. 1 (bottom). The results follow a stretched exponential trend as predicted by the theory of Zilman and Granek for membrane bending fluctuations in which the membranes are treated as thin elastic sheets.[58] To account for dynamic contributions from the diffusion of the vesicles, we fit the data with two contributions as described by I. Hoffman and presented in Eq 1.[59] The dynamic contribution from the vesicle diffusion was described by diffusion coefficient, D, as outlined by Hoffmann *et al.* and was independently determined for each sample using dynamic light scattering (DLS) (Table S4). The diffusion coefficients determined by DLS for each composition of the IMM, TOCL/POPC, and TOCL/POPE were 0.394 Å^2/ns, 0.398 Å^2/ns, and 0.452 Å^2/ns respectively. The resulting fits from Eq 1 are shown as solid lines in Figure 1 (bottom). From these fits, the corresponding decay rates for the membrane fluctuations, Γ_{ZG}, follow the expected Q^3-dependence shown in the inset in Figure 1 (bottom) with a slope that is inversely related to the effective bending modulus, $\widetilde{\kappa}$.[58]

The work done by Zilman and Granek was extended by Watson and Brown to account for the finite thickness of the bilayer because the membrane is not accurately described as a thin structureless sheet, and accounting for the dissipation within the bilayer is important on the nanometer length scale and nanosecond time scales measured with NSE.[37,38] Their work showed that the effective bending modulus, $\widetilde{\kappa}$, measured by NSE is related to the intrinsic bending modulus, κ, through Eq 2. The obtained κ values for all compositions with varying PST concentrations are shown in Fig 2. We observed significant increase in bending rigidity with added PST in the IMM-mimic (≈57.5%) and (≈40.2%) in the CL/PE mimic with added PST. These values have not been previously reported in literature and consequently cannot be compared; however, certain conclusions can be drawn when compared to LUVs composed

of POPE and POPC compositions. The addition of TOCL to membranes composed of POPE and POPC has a membrane ordering effect and increases membrane rigidity in PC membranes.[60–63] In extension, the present data show the addition of PST slows down the membrane dynamics and increaes κ in the studied LUV compositions as measured by NSE (Table 2). This increase in $\widetilde{\kappa}$ suggests PST has a stiffening effect greater than that of TOCL alone on the IMM mimic and other compositions.

Structure of IMM-mimic Vesicles

The structural parameters of the IMM-mimic, POPE/TOCL and POPC/TOCL vesicles were analyzed by joint refinement of small angle neutron scattering (SANS) and small angle x-ray scattering (SAXS) which offer complementary structural information (Table S1) by taking advantage of the different contrasts provided by neutrons and x-rays. To obtain real space information from these techniques where usable information like the bilayer thickness and area per lipid are present, a model based scattering density profile (SDP) was used to parse the membrane bilayer into three distinct segments.[35,64,65] The volume probabilities are shown in Figure 3A.

The structural information obtained from SANS and SAXS provides insight on PST's effect on bilayer structure and additional insights into the bending rigidity results in a concentration dependant manner shown in Table 2. Using 100% D_2O and fully protiated LUVs the contrast between the bulk aqueous solvent and the bilayer composition is exploited using SANS to highlight the total bilayer thickness as seen in Fig 3B. Whereas the SAXS data inset Fig 3 demonstrate a different bilayer thickness, specifically the electron dense phosphate-to-phosphate thickness (D_{HH}) of opposing bilayer leaflets.

The addition of PST increases the total bilayer thickness by $\approx$1 Å as seen by a shift in the local scattering minima (q_{min}) near 0.15 Å^{-1}. This suggests that at the measured concentrations PST has minimal effect on bilayer thickness, as observed by a minor ($< 2.7\%$) increase in the structural parameters D_B, D_{HH}, and $2D_C$ (Table 2).

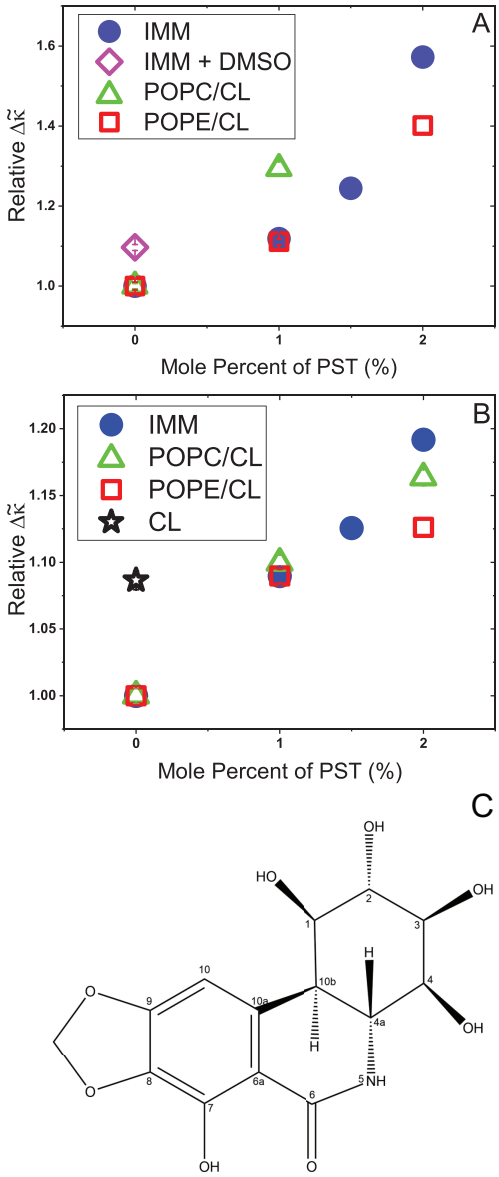

Figure 2: (A) Relative bending modulus ($\Delta\widetilde{\kappa} = \widetilde{\kappa}_{PST}/\widetilde{\kappa}_{pure}$) for varying concentrations of PST at 37 °C, IMM (◯, *blue*), POPE/CL (□, *red*), POPC/CL (△, *green*), and IMM w/DMSO-d-6 (◊, *magenta*) measured by NSE experiments. (B) Relative bending modulus ($\Delta\widetilde{\kappa} = \widetilde{\kappa}_{PST}/\widetilde{\kappa}_{pure}$) for varying concentrations of PST at 37 °C, IMM (◯, *blue*), POPE/CL (□, *red*), POPC/CL (△, *green*), and CL (★, *black*) calculated by MD simulations. (C) Structure of Pancratistatin (PST).

It is also important to note that DMSO was needed to introduce PST into the liposomal suspension due to PST's hydrophobic nature. DMSO is known to have a dehydrating effect on lipid bilayers leading to a weakening of hydrogen bonds between lipid headgroups and water molecules.[66] This known effect has been shown to lead to faster solvation dynamics

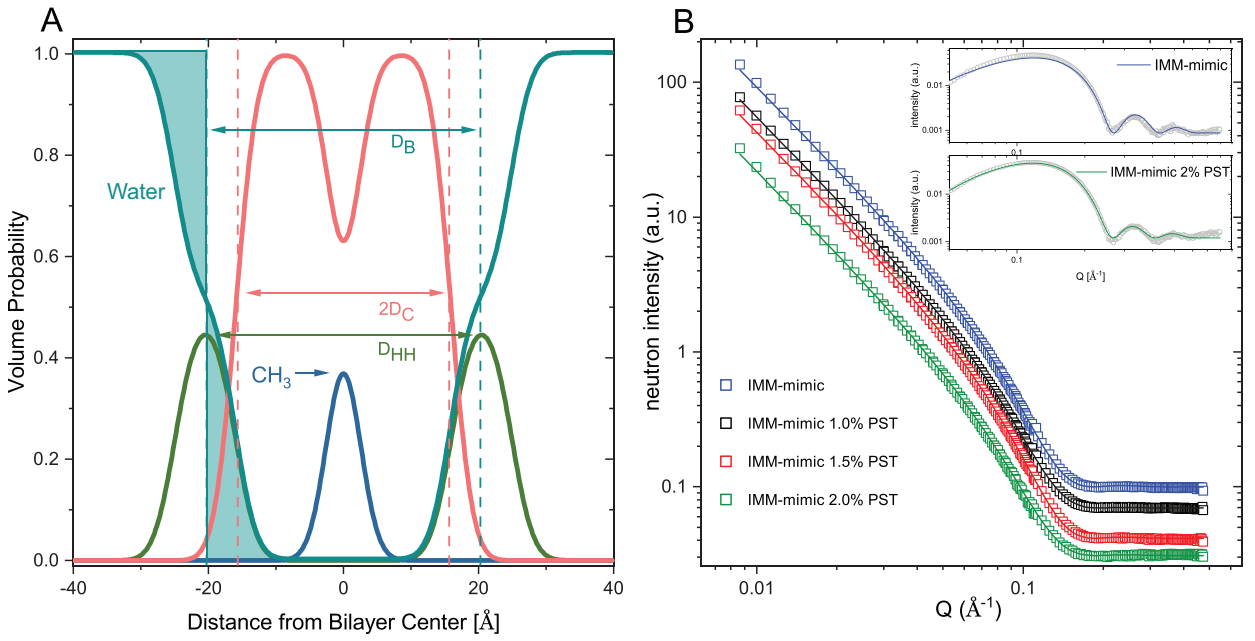

Figure 3: (A) Volume probability distribution for the IMM-mimic bilayer, where the total probability is equal to 1 at each point along the bilayer normal. The water distribution is represented by the teal line, the headgroup region by the green line, the hydrocarbon chain (CH, CH_2) by the red line, and the terminal methyl (CH_3) by the blue line. (B) Structure of symmetric IMM-mimic vesicles with increasing PST concentration given by experimental SANS form factors (□) and fits (solid lines). Data is offset for greater visibility. Inset (top) structure of symmetric IMM-mimic vesicles with and without PST given by experimental SAXS form factors (◯) and fits (solid lines).

Table 2: Structural parameters of various compositions obtained from NSE spectroscopy and generated from SDP model analysis of experimental (EXP) data and unrestrained MD simulations. Where κ is the bending rigidity, A_L is the area per lipid, D_B is the total bilayer thickness, D_{HH} is the phosphate-to-phosphate thickness, and $2D_C$ represents the carbon chain length.

Composition	Structural Parameters				
	κ ($\kappa_B T$)	A_L (Å^2)	D_B (Å)	D_{HH} (Å)	$2D_C$ (Å)
IMM Mimic (EXP)	28.0 ± 0.9	80.9 ± 0.2	40.6 ± 0.5	41.0 ± 0.5	31.3 ± 0.4
IMM Mimic w/ 1.0% PST (EXP)	31.4 ± 1.0	79.8 ± 0.3	40.9 ± 0.5	41.1 ± 0.3	31.2 ± 0.2
IMM Mimic w/ 1.5% PST (EXP)	34.9 ± 0.9	79.4 ± 0.4	41.3 ± 0.2	41.6 ± 0.4	31.9 ± 0.3
IMM Mimic w/ 2.0% PST (EXP)	44.1 ± 1.9	78.2 ± 0.3	41.7 ± 0.3	42.1 ± 0.3	32.6 ± 0.2
IMM Mimic (MD)	33.4 ± 0.7	79.3 ± 0.1	41.0 ± 0.1	41.5 ± 0.1	31.9 ± 0.1
IMM Mimic w/ 1.0% PST (MD)	36.4 ± 0.6	79.1 ± 0.1	41.6 ± 0.1	41.6 ± 0.1	32.1 ± 0.1
IMM Mimic w/ 1.5% PST (MD)	37.6 ± 0.6	78.8 ± 0.1	41.9 ± 0.1	42.3 ± 0.1	32.2 ± 0.1
IMM Mimic w/ 2.0% PST (MD)	39.8 ± 0.6	78.4 ± 0.1	42.8 ± 0.1	42.8 ± 0.3	32.7 ± 0.1
IMM Mimic w/ 2.0% DMSO (EXP)	30.8 ± 0.8	80.3 ± 0.2	40.7 ± 0.5	41.1 ± 0.7	31.6 ± 0.4

due to a decrease in the bilayer rigidity.[67] From our results, the opposite is true for bilayer rigidity, as DMSO stiffened the membrane slightly ($\approx 10\%$). While our results suggested that DMSO addition slightly stiffened the membranes, the increase in $\widetilde{\kappa}$ from the carrier solvent was several times lower than of PST plus DMSO. This suggests the bulk effect of membrane stiffening comes from PST and not DMSO. Ultimately, the volume of DMSO had no substantial effect on the other structural parameters and the primary stiffening effect was due to the addition of PST as seen in Table 2.

PST *in Silico*

To investigate in more detail the effects of PST on membrane properties, we performed Molecular Dynamics (MD) simulations of the IMM-mimic, as well as the TOCL, TOCL/POPC and TOCL/POPE bilayers mimicking the experimental conditions. We first compared the structural parameters calculated from the simulations to those obtained from the scattering experiments (Tables 1 and S3). There was good overall agreement between the corresponding areas per lipid and various bilayer thicknesses both for the systems with and without PST; importantly, the trends upon increasing PST concentration were reproduced. We then calculated the bending moduli by analyzing the fluctuations in lipid splay angles.[51–53] The MD results qualitatively reproduced the experimentally observed increase in membrane rigidity with increasing PST concentration, though we note that the κ values extracted from the MD measurements differed from the NSE measurements by 11% on average (Tables 2 and S5)

We then set off to perform a more in-depth analysis of the simulated lipid dynamics and organization. The first parameter that was assessed was the acyl chain order parameters (S_{CH}). As S_{CH} provides structural and dynamic information of each carbon along the acyl chain, taken as an ensemble, S_{CH} captures key factors that qualitatively define the bilayer fluidity. Therefore, we can extrapolate the effects of PST to the overall membrane fluidity. Moreover, S_{CH} provides information on the overall order of the membrane and can be extended to understand drug-membrane interactions.[68,69]

Using Eq. 5

$$S_{\mathrm{CH}} = \frac{3}{2}\langle \cos^2\theta \rangle - \frac{1}{2} \tag{5}$$

where θ is the angle between the C-H bond vector and the bilayer normal and the angled brackets represent molecular and temporal averages, we can describe the average orientation of the C-H bonds with respect to the bilayer normal for all chain carbons of a specific lipid.[70] The magnitude of S_{CH} is directly proportional to acyl chain order where a more ordered chain will have a greater $|S_{\mathrm{CH}}|$ value as seen in Fig 4.

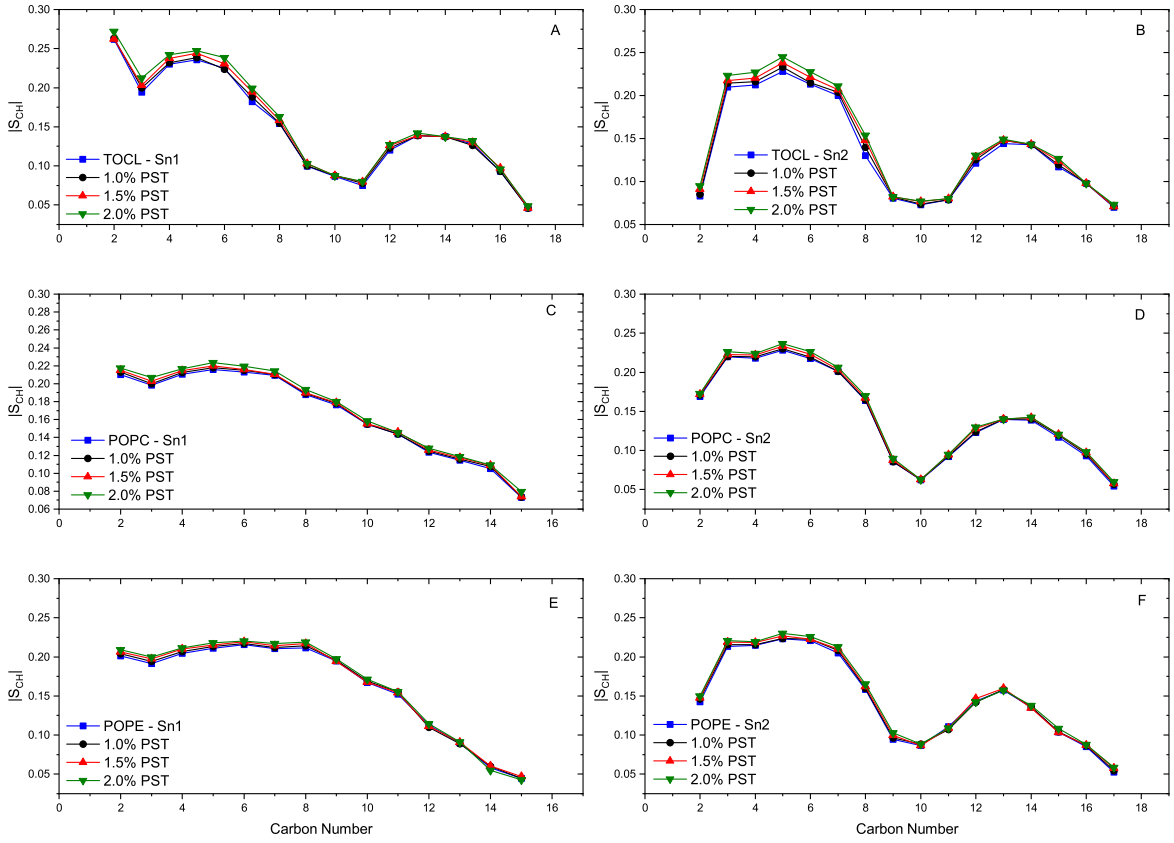

Figure 4: Acyl chain order parameters from MD simulations of the IMM with increasing concentration of PST. (A) TOCL-sn1 (B) TOCL-sn2 (C) POPC-sn1 (D) POPC-sn2 (E) POPE-sn1 and (F) POPE-sn2. The graphical abstract displays these findings in more detail, illustrating the stiffening effects of PST to the IMM mimic.

The order parameter profiles of our baseline compositions were in good agreement with analogous values reported in the literature.[71–73] Analysis of the PST-containing systems

showed that the effects of PST are most notable for the carbons closer to the glycerol backbone as shown by the increase in S_{CH} with increasing PST concentration; this indicates that C2-C8 for both sn1 and sn2 chains of TOCL are the most affected by the presence of PST. Though POPE and POPC see an increase in acyl chain order between C2-C8, the extent to which they are affected is lower. This suggests that PST has a greater affinity towards TOCL as well as an ordering effect on the hydrocarbon chains. The ordering of the hydrocarbon chains as seen by the increase in S_{CH} agrees with the increase in κ, as an increase in hydrocarbon chain order is seen as the membrane stiffens.[74]

MD simulations were additionally used to further explore the localization of PST relative to the membrane. Understanding how a drug interacts with the membrane is vital to elucidating how it functions with respect to biological events and how it influences membrane properties.[75–77] To determine where PST localizes, the density of PST was averaged over 500 ns of each simulation containing PST.

In Fig 5A, PST density is plotted against the distance from the bilayer centre for the IMM-mimic: PST is primarily concentrated on the lipid bilayer surface as the density peak values are between 21 (Å) to 23 (Å) which is roughly half the values of D_B and D_{HH} reported in Table 2. This further suggests PST localizes at the membrane surface regardless of composition and has a higher binding affinity to the membrane than the surrounding aqueous environment.

Lastly, the association between PST and specific lipid species was investigated as recent work shows that some drug therapeutics have greater affinity towards specific lipid species.[76,77] To investigate whether PST associates with one lipid species more than another, the radial distribution function (RDF), $g(r)$, between PST and each lipid species in the IMM-mimic was calculated for all PST-containing simulations. The RDF describes how the density of surrounding matter varies as a function of the distance from a defined point. For the MD simulations, PST was added to the aqueous solvent in a random fashion to mirror the *in vitro* experiments. Consequently, if PST were to closely associate with a particular

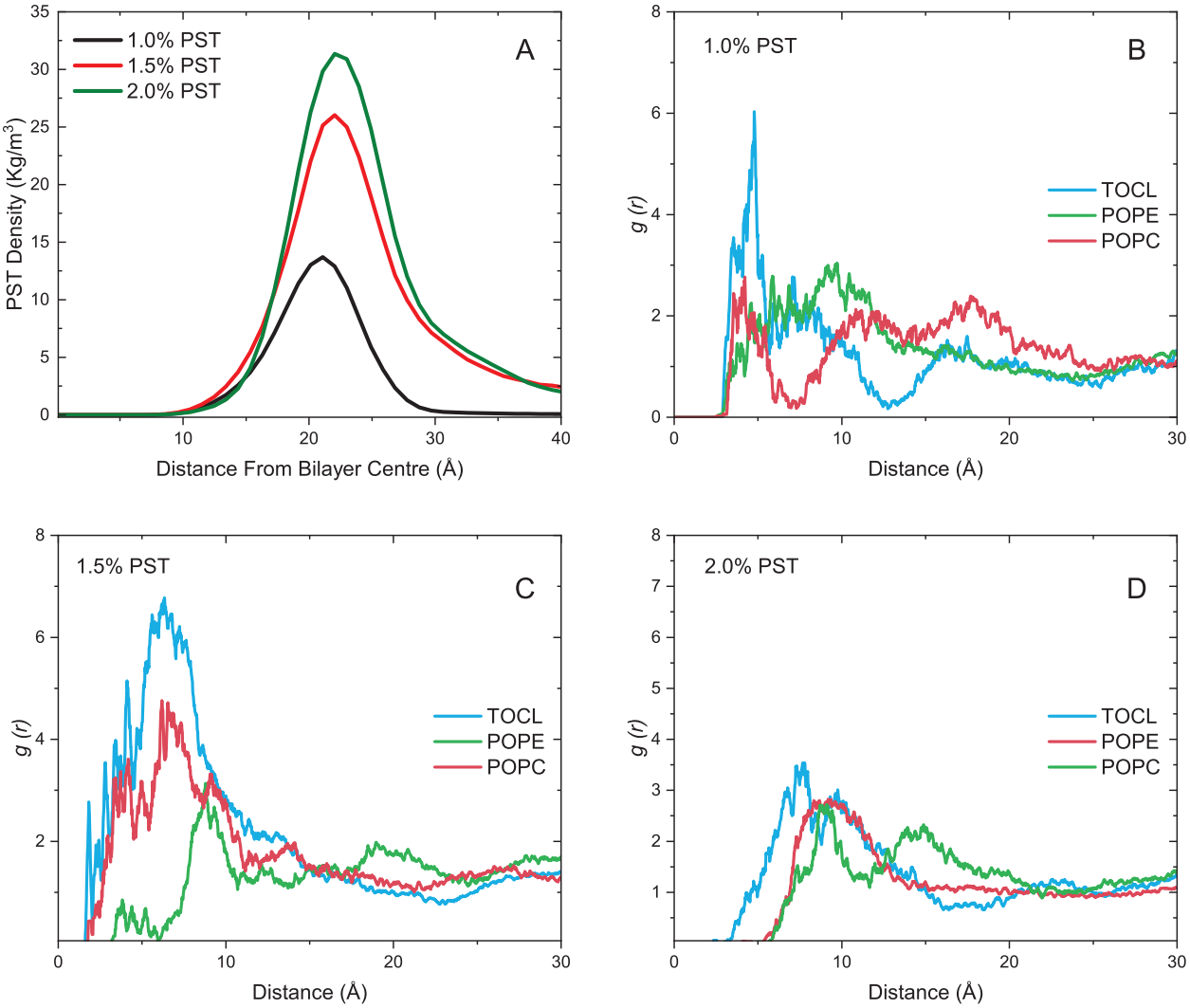

Figure 5: PST density profiles obtained from MD runs for the IMM-mimic with (A) 1%, 1.5%, and 2% mol of PST. The maximum amplitude for each curve is 21, 21, and 22 (Å) for increasing order of PST concentration. Radial distribution function graphs for MD-simulated IMM-mimics were used to investigate PST's affinity towards lipid headgroups with (B) 1.0%, (C) 1.5%, and (D) 2.0% PST. The RDFs were computed by analyzing the distances between the centers of mass of PST and the lipid headgroups. A moving average over 5 bins is used to increase smoothness of the curves. The graphical abstract illustrates these findings, displaying the binding preference of PST to CL more clearly.

lipid species, it would be fair to reason that the particular lipid species is of significance to PST's functionality. By defining the points of interest as the centre of mass of PST and the headgroups, the RDFs were calculated over the duration of each simulation, resulting in a plot of $g(r)$ vs. distance, as seen in Fig 5. The graphs represent the change in density of

a specific lipid headgroup over a certain distance from a PST molecule. The RDF results demonstrate PST has a higher affinity towards TOCL compared to POPE or POPC as seen in Fig 5B-D. As CL only accounts for a mole fraction of 25% of the IMM mimic, when combined with the previous density results, it is clear that PST interacts preferentially with the headgroups of CL.

Discussion

The structure of mitochondria is key to regulation and function in healthy cells. An alteration in mitochondrial structure is directly related to cells undergoing apoptosis.[78] Nonetheless, studies have put considerable effort into investigating PST and its effect on proteins within the mitochondria and not the physical properties of the mitochondria themselves.[79] Considering PST is a pro-apoptotic agent, physical alterations of the mitochondrial membrane by PST must be investigated and more specifically the interactions between PST and CL, a lipid almost exclusive to the inner mitochondrial membrane. In the presented work, we observed a significant increase in bending rigidity with added PST in the IMM-mimic ($\approx$57.5%) and in the CL/PE mimic ($\approx$40.15%) via NSE as seen in Fig 2. In contrast, PST had minimal effect on the structural parameters D_B, D_{HH}, $2D_C$, and a small ($< 3.5\%$) effect on the A_L (Table 2). This would suggest PST does not insert itself into the bilayer but rather interacts with the surface of the membrane as shown by the area per lipid (A_L) and κ values. However, whether PST sits asymmetrically or crosses the bilayer remains unknown. Work done by Marquardt *et al.*, probed the effect of transvere lipid organization and its role in controlling bending fluctuations.[60] Their work revealed that asymmetric bilayers exhibited a larger bending modulus than that of symmetric bilayers due to the asymmetric distribution of lipids in the inner and outer leaflet. This raises the matter of whether PST localizes on the outer or inner membrane or is distributed asymmetrically. To answer this, further research is required on the localization of PST on the outer and inner membrane. A_L for

the IMM-mimic decreased at 2 mole percent of PST both in the experiments ($\approx 3.39\%$) and MD simulations ($\approx 1\%$) as shown in Table 2. This decrease in A_L can largely be attributed to the structure of PST as seen in Fig 2C and its stiffening effects on the bilayer as seen by the increase in κ, seen more clearly in Fig 2. This trend of a seemingly large increases in κ along with small decreases in A_L has been previously observed by Kelley *et al.*, with mixtures of dimyristoylphosphatidylcholine (DMPC) (14:0 diC) and distearoylphosphatidylcholine (DSPC) (18:0 diC) as determined by NSE and SANS.[80] An explanation for this strong dependence of κ on A_L is offered by the theory that predicts κ is strongly dependent on A_L and more specifically, is associated to the conformational entropy of the tails .[81] The theory proposes that as the area per chain in the bilayer decreases, the number of conformations available to the tail decreases, thus making the membrane harder to bend. Considering this, PST potentially acts to reduce conformational degrees of freedom, consequently increasing the bending rigidity of IMM mimic. Altogether PST is a planar molecule, it induces order, increases bilayer thickness and is considerably hydrophobic. The steric hindrance introduced by the molecule has ordering effects like that of cholesterol, but unlike cholesterol, PST acts on the surface of the bilayer.

MD simulations provided additional details about the effects of PST that would be otherwise unattainable by traditional characterization techniques. The structural parameters D_B, D_{HH}, $2D_C$, and A_L from the MD simulations were all in good agreement, ($< 1.9\%$ difference) with values obtained from joint refinement of experimental scattering data, validating the simulation trajectories. There was some variance in the bending moduli (κ) calculated from the MD simulations and measured with NSE. The values obtained by both techniques exhibit the same trend in that increasing PST concentration increases the bending modulus, further seen in Fig 2. For the IMM-mimic the addition of 2% PST led to an increase in bending rigidity of ($\approx$57.5%) for the NSE measurement and ($\approx$19.2%) for the simulated bilayer. This difference is present in the TOCL/POPE composition where the addition of 2% PST resulted in ($\approx$40.1%) for the experimental system and ($\approx$12.6%) for the simulated one. The

discrepancies in the absolute changes of (κ) could be due to some of the technical challenges in the computational analysis of bending rigidity in bilayer mixtures containing TOCL. In particular, the algorithm relies on the analysis of splay angles of only neighboring lipids that are defined by a single distance cutoff.[51–53] Due to the larger area per lipid of TOCL relative to that of phospholipids, identifying such uniform distance metric becomes inherently difficult. Further advancements in the algorithm such as allowing for variable distance cutoffs in the definition of neighboring lipids could help improve the agreement between NSE and simulations for TOCL-containing mixtures. For the purpose of this work, the relative trend in κ with the addition of PST is more representative than the absolute values due to the simplicity of the mimic systems as compared to biology.

Another possible reason for the discrepancy in the values of κ extracted from the NSE and MD simulations is that these techniques extract the membrane rigidity based on fundamentally different measurement principles. NSE works in the time domain, where the relaxation rate of the membrane fluctuations is related to the membrane rigidity as well as the dissipation through the surrounding solvent and within the membrane itself. The Watson and Brown theory relating effective bending modulus $\widetilde{\kappa}$ to the intrinsic bending modulus κ takes into account leaflet density and interleaflet friction.[37] This means the redistribution of lipids do not fully relax within the time scale of the fluctuations, which leads to an effectively larger bending rigidity at the nanoscale. The greater increase in κ measured with NSE compared to the MD results in Figure 2 may suggest that adding PST affects the internal dissipation within the membrane, leading to an even greater increase in the effective rigidity that influences the local membrane fluctuations. The results from the NSE experiment (Table 2) suggest that the addition of PST to the system greatly increases membrane order and decreases membrane fluidity, all of which are fundamentally linked to oxidative phosphorylation.[82–84] Rearrangement of mitochondrial phospholipids leads to the uncoupling of oxidative phosphorylation and destabilizes proteins required for the function of the electron transport chain (ETC) proteins embedded within the mitochondrial membrane.[85,86] More so,

the interaction between CL and cytochrome c and its role in apoptosis is highly dependant on lipid organization and fluidity.[24] With this, our results relate PST-induced mitochondrial apoptosis by correlating increased membrane rigidity and reduced fluidity to decreased mitochondrial membrane functionality.

With the aid of MD simulations, three key findings were suggested: (i) PST is primarily concentrated on the membrane surface, (ii) PST has greater affinity for CL than PE or PC lipid headgroups, (iii) and PST has an ordering effect on C2-C8 for both the sn1 and sn2 chains of CL. This indicates that PST not only targets CL, but also localizes on the membrane surface and creates order with the hydrocarbon region of CL by interacting with the carbons closest to the glycerol backbone. In literature, cytochrome c has been shown to anchor to CL via electrostatic interactions and hydrogen bonding, and its release from CL is sufficient to initiate apoptosis.[87] Displacement of cytochrome c from CL primarily occurs due to oxidative degradation of CL hydrocarbon tails and causes a disruption of the molecular interactions between the membrane lipid and the protein.[88] Furthermore, work has shown that cytochrome c binds to CL in a so-called extended lipid conformation. This occurs when a single acyl tail is perpendicular to the membrane plane and embedded within a hydrophobic cavity of cytochrome c, leaving the other acyl tail embedded in the membrane.[89] The extended lipid conformation has been confirmed with both NMR and X-ray studies and explains how cytochrome c is anchored to the membrane.[90,91] This results in a hydrophobic interaction between cytochrome c and the membrane surface without penetration into the bilayer.[92]

In the MD simulations, PST not only has greater affinity for CL compared to PE and PC but also increases acyl chain order of sn1 and sn2, and decreases overall membrane fluidity as shown by the S_{CH} results in Fig 4 and broadly supported by the lateral diffusion results shown in (Table S2). By localizing on the surface of the membrane, the addition of 2% PST decreases the area per lipid and maintains a bilayer thickness close to 41 Å(D_{HH}), potentially opposing the ability of cytochrome c to create bilayer disorder/deformation and increase

membrane thickness (D_{HH}).[91] Additionally, the mitochondria of cancerous cells have a pH value of ≈8, while the pKa of PST is 7.7, leading to the deprotonated form of PST to exist within the mitochondria.[93] As Rytomaa *et al.*, have discovered, an acidic pH environment leads to a tighter bond between cytochrome *c* and the membrane due to both electrostatic and hydrogen bonding, while at neutral pH, cytochrome *c* associates only electrostatically and can be easily displaced by increasing ionic concentration.[94] Therefore, for PST to displace cytochrome *c* within a cancerous cell, it must only overcome electrostatic interactions and can neglect the effects of hydrogen bonding. Thus by adding PST, the conditions needed by cytochrome *c* to remain anchored are possibly sufficiently disrupted which could lead to the release of some cytochrome *c* —initiating the apoptotic cascade.

Membrane fluidity is of great interest in relation to membrane proteins and their optimal conformation for catalytic activity such as in the ETC.[95] The structural data obtained from NSE, SAXS/SANS, and supplemented via MD simulations show PST has minimal effect on bilayer thickness, some effect on A_L, and a substantial effect on bending rigidity. Proteins, such as the ones in the ETC, are sensitive to even a slight deviation from their homeostatic state, leading to a cascade of complications in relation to energy production and cell survival.[96] Protein content within the membrane is related to bending rigidity, where an increase in the protein and peptide density in many membrane systems can either reduce the rigidity or increase the rigidity.[74,97] The IMM is composed of a ratio approximately (4 : 1) proteins:lipids, suggesting that the IMM naturally has low membrane rigidity.[98] With the addition of 2% PST to the IMM-mimic, there was an increase of (≈57.5%) in the bending rigidity value, potentially affecting the efficiency and viability of the ETC.

Hackenbrock *et al.*, have thoroughly investigated the effect of diffusion in the mitochondrial ETC and have produced a few key findings. First, electron transport in the ETC is a long range obstructed diffusion-coupled kinetic process, and second, the rates of diffusion of the redox components have a direct influence on the kinetic process of electron transport and are rate limiting as in diffusion control.[99] Regarding the first finding, there must be a

low resistance to motion in the bilayer as there are a number of nonspecific protein-protein collisions required for the ETC to function properly. The IMM offers such conditions as a cholesterol-free and highly unsaturated phospholipid bilayer. Shown by the MD simulations in Fig 4 and the lateral diffusion results shown in (Table S2), PST has an ordering effect on the hydrocarbon chains. This reduces the free movement of lipid tails, suggesting an increase in resistance to motion in the bilayer, affecting the rate of the ETC as shown for obstructed long range diffusion in biomembranes.[100] The second key finding of Hackenbrock *et al.* demonstrates that electron transport in the IMM is a diffusion-coupled kinetic process, where electron transport is limited by the rate of lateral diffusion of proteins, specifically electron carriers. By using the theory of Reister and Seifert to explain lateral diffusion of proteins in a fluctuating membrane, the relationship between bending rigidity and free diffusing proteins becomes inherently clear and allows for an explanation for a slowed down and disrupted ETC.[101]

Reister and Seifert attribute the difference between the actual intramembrane and the measured projected diffusion constant to membrane fluctuations, where a decrease in bending rigidity leads to a softer membrane and an increase in true intramembrane diffusion. Similarly, as the bending rigidity of a membrane increases, there is a decrease in diffusion for free diffusing proteins such as the electron carriers in the ETC. By combining the theory of Reister and Seifert with the findings of Hackenbrock *et al.*, an explanation of how PST may affect the ETC forms. As the bending rigidity increases with increasing PST concentration, the rate of unbound protein diffusion decreases, reducing the kinetic processes of the ETC. This reduction in kinetic processes for the ETC can lead to an array of downstream effects related to mitochondrial dysfunction and apoptosis. The decrease in membrane fluidity may have an effect on cytochrome *c* as it is the only non-integral protein of the ETC. Its role in the ETC is to transfer electrons from complex III to complex IV and requires close association to CL to function optimally.[102] Recently Kalpage *et al.* have shown that the electron transfer from cytochrome *c* to complex IV is the rate limiting step of the ETC, putting more

importance on the proper function and execution of cytochrome *c*. This emphasizes that any dysregulation of the ETC can lead to mitochondrial membrane potential hyperpolarization, resulting in the release of cytochrome *c* and triggering apoptosis.[103]

Understanding the mechanism of how PST induces apoptosis in cancerous cells is crucial for the development of an efficacious and targeted treatment towards certain cancers. In this study, we utilized NSE spectroscopy to characterize the bending rigidity of an inner mitochondrial membrane mimic incubated with PST. MD simulations were used to extrapolate fluidity and order of the membrane mimic and establish PST localization and preference within the bilayer. We report that PST increased bilayer rigidity by approximately 57%, increased acyl chain order within the membrane, preferentially associated with cardiolipin, and led to decreased fluidity within the membrane. Although these observed effects were for model membranes lacking mitochondrial proteins, these effects would have a considerable impact on vital processes which regulate apoptosis within the mitochondria. Our data suggest that by increasing membrane rigidity, decreasing membrane fluidity, and preferentially interacting with cardiolipin, PST may have a direct effect on the efficacy of cytochrome *c* and electron transport chain function, inducing optimal conditions for initiation of apoptosis.

References

(1) Nussbaumer, S.; Bonnabry, P.; Veuthey, J. L.; Fleury-Souverain, S. Analysis of anticancer drugs: A review. *Talanta* **2011**, *85*, 2265–2289.

(2) Boukalova, S.; Rohlenova, K.; Rohlena, J.; Neuzil, J. *Mitochondrial Biology and Experimental Therapeutics*; Springer International Publishing, 2018; pp 613–635.

(3) McLachlan, A.; Kekre, N.; McNulty, J.; Pandey, S. Pancratistatin: A natural anticancer compound that targets mitochondria specifically in cancer cells to induce apoptosis. *Apoptosis* **2005**, *10*, 619–630.

(4) Pettit, G. R.; Gaddamidi, V.; Cragg, G. M.; Herald, D. L.; Sagawa, Y. Isolation and structure of pancratistatin. *Journal of the Chemical Society, Chemical Communications* **1984**, 1693–1694.

(5) Pandey, S.; Kekre, N.; Naderi, J.; McNulty, J. Induction of apoptotic cell death specifically in rat and human cancer cells by pancratistatin. *Artificial Cells, Blood Substitutes, and Immobilization Biotechnology* **2005**, *33*, 279–295.

(6) Griffin, C.; McNulty, J.; Pandey, S. Pancratistatin induces apoptosis and autophagy in metastatic prostate cancer cells. *International Journal of Oncology* **2011**, *38*, 1549–1556.

(7) Ceriotti, G. Narciclasine: An antimitotic substance from narcissus bulbs [18]. *Nature* **1967**, *213*, 595–596.

(8) Pellegrino, S.; Meyer, M.; Zorbas, C.; Bouchta, S. A.; Saraf, K.; Pelly, S. C.; Yusupova, G.; Evidente, A.; Mathieu, V.; Kornienko, A.; Lafontaine, D. L.; Yusupov, M. The Amaryllidaceae Alkaloid Haemanthamine Binds the Eukaryotic Ribosome to Repress Cancer Cell Growth. *Structure* **2018**, *26*, 416–425.e4.

(9) Fürst, R. Narciclasine - an Amaryllidaceae Alkaloid with Potent Antitumor and Anti-Inflammatory Properties. *Planta Medica* **2016**, *82*, 1389–1394.

(10) Şener, B.; Orhan, I.; Satayavivad, J. Antimalarial Activity Screening of Some Alkaloids and the Plant Extracts from Amaryllidaceae. *Phytotherapy Research* **2003**, *17*, 1220–1223.

(11) Kekre, N.; Griffin, C.; McNulty, J.; Pandey, S. Pancratistatin causes early activation of caspase-3 and the flipping of phosphatidyl serine followed by rapid apoptosis specifically in human lymphoma cells. *Cancer Chemotherapy and Pharmacology* **2005**, *56*, 29–38.

(12) Griffin, C.; Hamm, C.; Mcnulty, J.; Pandey, S. Pancratistatin induces apoptosis in clinical leukemia samples with minimal effect on non-cancerous peripheral blood mononuclear cells. *Cancer Cell International* **2010**, *10*, 6.

(13) Henry-Mowatt, J.; Dive, C.; Martinou, J. C.; James, D. Role of mitochondrial membrane permeabilization in apoptosis and cancer. *Oncogene* **2004**, *23*, 2850–2860.

(14) Mayer, B.; Oberbauer, R. Mitochondrial Regulation of Apoptosis. *Physiology* **2003**, *18*, 89–94.

(15) Cai, J.; Yang, J.; Jones, D. P. Mitochondrial control of apoptosis: The role of cytochrome c. *Biochimica et Biophysica Acta - Bioenergetics* **1998**, *1366*, 139–149.

(16) Scorrano, L.; Ashiya, M.; Buttle, K.; Weiler, S.; Oakes, S. A.; Mannella, C. A.; Korsmeyer, S. J. A distinct pathway remodels mitochondrial cristae and mobilizes cytochrome c during apoptosis. *Developmental Cell* **2002**, *2*, 55–67.

(17) Zhivotovsky, B.; Orrenius, S.; Brustugun, O. T.; Doskeland, S. O. Injected cytochrome C induces apoptosis [4]. *Nature* **1998**, *391*, 449–450.

(18) Jiang, X.; Wang, X. Cytochrome C-Mediated Apoptosis. *Annual Review of Biochemistry* **2004**, *73*, 87–106.

(19) Ott, M.; Zhivotovsky, B.; Orrenius, S. Role of cardiolipin in cytochrome c release from mitochondria. *Cell Death and Differentiation* **2007**, *14*, 1243–1247.

(20) Kagan, V. E.; Bayir, H. A.; Belikova, N. A.; Kapralov, O.; Tyurina, Y. Y.; Tyurin, V. A.; Jiang, J.; Stoyanovsky, D. A.; Wipf, P.; Kochanek, P. M.; Greenberger, J. S.; Pitt, B.; Shvedova, A. A.; Borisenko, G. Cytochrome c/cardiolipin relations in mitochondria: a kiss of death. *Free Radical Biology and Medicine* **2009**, *46*, 1439–1453.

(21) Orrenius, S.; Zhivotovsky, B. Cardiolipin Oxidation Sets Cytochrome C Free. *Nature Chemical Biology* **2005**, *1*, 188–189.

(22) Kagan, V. E. et al. Cytochrome C Acts As A Cardiolipin Oxygenase Required for Release of Proapoptotic Factors. *Nature Chemical Biology* **2005**, *1*, 223–232.

(23) Schug, Z. T.; Gottlieb, E. Cardiolipin acts as a mitochondrial signalling platform to launch apoptosis. *Biochimica et Biophysica Acta - Biomembranes* **2009**, *1788*, 2022–2031.

(24) Gonzalvez, F.; Gottlieb, E. Cardiolipin: Setting the beat of apoptosis. *Apoptosis* **2007**, *12*, 877–885.

(25) Dipasquale, M.; Gbadamosi, O.; Nguyen, M. H.; Castillo, S. R.; Rickeard, B. W.; Kelley, E. G.; Nagao, M.; Marquardt, D. A Mechanical Mechanism for Vitamin e Acetate in E-cigarette/Vaping-Associated Lung Injury. *Chemical Research in Toxicology* **2020**, *33*, 2432–2440.

(26) Nagao, M.; Kelley, E. G.; Faraone, A.; Saito, M.; Yoda, Y.; Kurokuzu, M.; Takata, S.; Seto, M.; Butler, P. D. Relationship between Viscosity and Acyl Tail Dynamics in Lipid Bilayers. *Physical Review Letters* **2021**, *127*, 078102.

(27) Kumari, P.; Faraone, A.; Kelley, E. G.; Benedetto, A. Stiffening Effect of the [Bmim][Cl] Ionic Liquid on the Bending Dynamics of DMPC Lipid Vesicles. *Journal of Physical Chemistry B* **2021**, *125*, 7241–7250.

(28) Lundbæk, J. A.; Birn, P.; Tape, S. E.; Toombes, G. E.; Søgaard, R.; Koeppe, R. E.; Gruner, S. M.; Hansen, A. J.; Andersen, O. S. Capsaicin regulates voltage-dependent sodium channels by altering lipid bilayer elasticity. *Molecular Pharmacology* **2005**, *68*, 680–689.

(29) Kuzmin, P. I.; Akimov, S. A.; Chizmadzhev, Y. A.; Zimmerberg, J.; Cohen, F. S. Line tension and interaction energies of membrane rafts calculated from lipid splay and tilt. *Biophysical Journal* **2005**, *88*, 1120–1133.

(30) Lucio, M.; Lima, J.; Reis, S. Drug-Membrane Interactions: Significance for Medicinal Chemistry. *Current Medicinal Chemistry* **2010**, *17*, 1795–1809.

(31) McAuley, K. E.; Fyfe, P. K.; Ridge, J. P.; Isaacs, N. W.; Cogdell, R. J.; Jones, M. R. Structural details of an interaction between cardiolipin and an integral membrane protein. *Proceedings of the National Academy of Sciences of the United States of America* **1999**, *96*, 14706–14711.

(32) Sorice, M.; Manganelli, V.; Matarrese, P.; Tinari, A.; Misasi, R.; Malorni, W.; Garofalo, T. Cardiolipin-enriched raft-like microdomains are essential activating platforms for apoptotic signals on mitochondria. *FEBS Letters* **2009**, *583*, 2447–2450.

(33) Glinka, C. J.; Barker, J. G.; Hammouda, B.; Krueger, S.; Moyert, J. J.; Orts∼, W. J. The 30 m Small-Angle Neutron Scattering Instruments at the National Institute of Standards and Technology. *J. Appl. Cryst* **1998**, *31*, 430–445.

(34) Kline, S. R. Reduction and analysis of SANS and USANS data using IGOR Pro. *Journal of Applied Crystallography* **2006**, *39*, 895–900.

(35) Lewis-Laurent, A.; Doktorova, M.; Heberle, F. A.; Marquardt, D. Vesicle Viewer: Online Analysis of Small Angle Scattering from Lipid Vesicles. *Biophysical Journal* **2021**, *120*, 4639–4648.

(36) Azuah, R. T.; Kneller, L. R.; Qiu, Y.; Tregenna-Piggott, P. L.; Brown, C. M.; Copley, J. R.; Dimeo, R. M. DAVE: A comprehensive software suite for the reduction, visualization, and analysis of low energy neutron spectroscopic data. *Journal of Research of the National Institute of Standards and Technology* **2009**, *114*, 341–358.

(37) Langer, S. A. Viscous modes of fluid bilayer membranes. *EPL* **1993**, *23*, 71–76.

(38) Watson, M. C.; Brown, F. L. Interpreting membrane scattering experiments at the mesoscale: The contribution of dissipation within the bilayer. *Biophysical Journal* **2010**, *98*, L9.

(39) Nagao, M.; Kelley, E. G.; Ashkar, R.; Bradbury, R.; Butler, P. D. Probing Elastic and Viscous Properties of Phospholipid Bilayers Using Neutron Spin Echo Spectroscopy. *Journal of Physical Chemistry Letters* **2017**, *8*, 4679–4684.

(40) Berendsen, H. J.; van der Spoel, D.; van Drunen, R. GROMACS: A message-passing parallel molecular dynamics implementation. *Computer Physics Communications* **1995**, *91*, 43–56.

(41) Klauda, J. B.; Venable, R. M.; Freites, J. A.; O'Connor, J. W.; Tobias, D. J.; Mondragon-Ramirez, C.; Vorobyov, I.; MacKerell, A. D.; Pastor, R. W. Update of the CHARMM All-Atom Additive Force Field for Lipids: Validation on Six Lipid Types. *Journal of Physical Chemistry B* **2010**, *114*, 7830–7843.

(42) Vanommeslaeghe, K.; Raman, E. P.; MacKerell Jr, A. D. Automation of the CHARMM General Force Field (CGenFF) II: assignment of bonded parameters and partial atomic charges. *Journal of chemical information and modeling* **2012**, *52*, 3155–3168.

(43) Vanommeslaeghe, K.; MacKerell Jr, A. D. Automation of the CHARMM General Force Field (CGenFF) I: bond perception and atom typing. *Journal of chemical information and modeling* **2012**, *52*, 3144–3154.

(44) Lee, J. et al. CHARMM-GUI Input Generator for NAMD, GROMACS, AMBER, OpenMM, and CHARMM/OpenMM Simulations Using the CHARMM36 Additive Force Field. *Journal of Chemical Theory and Computation* **2016**, *12*, 405–413.

(45) Berendsen, H. J.; Postma, J. P.; Van Gunsteren, W. F.; Dinola, A.; Haak, J. R. Molecular dynamics with coupling to an external bath. *The Journal of Chemical Physics* **1984**, *81*, 3684–3690.

(46) Bussi, G.; Donadio, D.; Parrinello, M. Canonical sampling through velocity rescaling. *Journal of Chemical Physics* **2007**, *126*, 014101.

(47) Parrinello, M.; Rahman, A. Polymorphic transitions in single crystals: A new molecular dynamics method. *Journal of Applied Physics* **1981**, *52*, 7182–7190.

(48) Braganza, L. F.; Worcester, D. L. Structural Changes in Lipid Bilayers and Biological Membranes Caused by Hydrostatic Pressure. *Biochemistry* **1986**, *25*, 7484–7488.

(49) Essmann, U.; Perera, L.; Berkowitz, M. L.; Darden, T.; Lee, H.; Pedersen, L. G. A smooth particle mesh Ewald method. *The Journal of Chemical Physics* **1998**, *103*, 8577.

(50) Humphrey, W.; Dalke, A.; Schulten, K. VMD: Visual molecular dynamics. *Journal of Molecular Graphics* **1996**, *14*, 33–38.

(51) Doktorova, M.; Harries, D.; Khelashvili, G. Determination of bending rigidity and tilt modulus of lipid membranes from real-space fluctuation analysis of molecular dynamics simulations. *Physical Chemistry Chemical Physics* **2017**, *19*, 16806–16818.

(52) Johner, N.; Harries, D.; Khelashvili, G. Erratum to: Implementation of a methodology for determining elastic properties of lipid assemblies from molecular dynamics simulations. *BMC Bioinformatics 2016 17:1* **2016**, *17*, 1–2.

(53) Johner, N.; Harries, D.; Khelashvili, G. Implementation of a methodology for determining elastic properties of lipid assemblies from molecular dynamics simulations. *BMC Bioinformatics 2016 17:1* **2016**, *17*, 1–11.

(54) Horvath, S. E.; Daum, G. Lipids of mitochondria. *Progress in Lipid Research* **2013**, *52*, 590–614.

(55) Schlame, M.; Otten, D. Analysis of cardiolipin molecular species by high-performance liquid chromatography of its derivative 1,3-bisphosphatidyl-2-benzoyl-sn-glycerol dimethyl ester. *Analytical Biochemistry* **1991**, *195*, 290–295.

(56) Schlame, M.; Ren, M.; Xu, Y.; Greenberg, M. L.; Haller, I. Molecular symmetry in mitochondrial cardiolipins. *Chemistry and Physics of Lipids* **2005**, *138*, 38–49.

(57) Kelley, E. G.; Butler, P.; Nagao, M. *Collective Dynamics in Model Biological Membranes Measured by Neutron Spin Echo Spectroscopy*; Walter de Gruyter, Inc., Boston, MA, 2019; pp 130–176.

(58) Zilman, A. G.; Granek, R. Undulations and dynamic structure factor of membranes. *Physical Review Letters* **1996**, *77*, 4788–4791.

(59) Hoffmann, I.; Michel, R.; Sharp, M.; Holderer, O.; Appavou, M.-S.; Polzer, F.; Farago, B.; Gradzielski, M. Softening of phospholipid membranes by the adhesion of silica nanoparticles-as seen by neutron spin-echo (NSE). *Nanoscale* **2014**, *6*, 6945–6952.

(60) Rickeard, B. W.; Nguyen, M. H. L.; DiPasquale, M.; Yip, C. G.; Baker, H.; Heberle, F. A.; Zuo, X.; Kelley, E. G.; Nagao, M.; Marquardt, D. Transverse lipid organization dictates bending fluctuations in model plasma membranes. *Nanoscale* **2020**, 10.1039.C9NR07977G.

(61) Kučerka, N.; Tristram-Nagle, S.; Nagle, J. F. Structure of Fully Hydrated Fluid Phase Lipid Bilayers with Monounsaturated Chains. *Journal of Membrane Biology* **2006**, *208*, 193–202.

(62) Arriaga, L. R.; López-Montero, I.; Monroy, F.; Orts-Gil, G.; Farago, B.; Hellweg, T. Stiffening Effect of Cholesterol on Disordered Lipid Phases: A Combined Neutron Spin Echo + Dynamic Light Scattering Analysis of the Bending Elasticity of Large Unilamellar Vesicles. *Biophysical Journal* **2009**, *96*, 3629–3637.

(63) Boscia, A. L.; Treece, B. W.; Mohammadyani, D.; Klein-Seetharaman, J.; Braun, A. R.; Wassenaar, T. A.; Klösgen, B.; Tristram-Nagle, S. X-ray structure, thermodynamics, elastic properties and MD simulations of cardiolipin/dimyristoylphosphatidylcholine mixed membranes. *Chemistry and Physics of Lipids* **2014**, *178*, 1–10.

(64) Kučerka, N.; Heberle, F. A.; Pan, J.; Katsaras, J. Structural significance of lipid diversity as studied by small angle neutron and X-ray scattering. *Membranes* **2015**, *5*, 454–472.

(65) Heberle, F. A.; Pan, J.; Standaert, R. F.; Drazba, P.; Kučerka, N.; Katsaras, J.; Heberle, F. A.; Pan, Á. J.; Katsaras, Á. J.; Standaert, R. F.; Drazba, P.; Kučerka, N.; Katsaras, J. Model-based approaches for the determination of lipid bilayer structure from small-angle neutron and X-ray scattering data. *Eur Biophys J* **2012**, *41*, 875–890.

(66) Cheng, C. Y.; Song, J.; Pas, J.; Meijer, L. H.; Han, S. DMSO Induces Dehydration near Lipid Membrane Surfaces. *Biophysical Journal* **2015**, *109*, 330–339.

(67) Kundu, S.; Malik, S.; Ghosh, M.; Nandi, S.; Pyne, A.; Debnath, A.; Sarkar, N. A Comparative Study on DMSO-Induced Modulation of the Structural and Dynamical Properties of Model Bilayer Membranes. *Langmuir* **2021**, *37*, 2065–2078.

(68) Piggot, T. J.; Allison, J. R.; Sessions, R. B.; Essex, J. W. On the Calculation of Acyl Chain Order Parameters from Lipid Simulations. *Journal of Chemical Theory and Computation* **2017**, *13*, 5683–5696.

(69) Khadka, N. K.; Cheng, X.; Ho, C. S.; Katsaras, J.; Pan, J. Interactions of the Anticancer Drug Tamoxifen with Lipid Membranes. *Biophysical Journal* **2015**, *108*, 2492–2501.

(70) Vermeer, L. S.; De Groot, B. L.; Réat, V.; Milon, A.; Czaplicki, J. Acyl chain order parameter profiles in phospholipid bilayers: Computation from molecular dynamics simulations and comparison with 2H NMR experiments. *European Biophysics Journal* **2007**, *36*, 919–931.

(71) Ferreira, T. M.; Coreta-Gomes, F.; Samuli Ollila, O. H.; Moreno, M. J.; Vaz, W. L.; Topgaard, D. Cholesterol and POPC segmental order parameters in lipid membranes: Solid state 1H-13C NMR and MD simulation studies. *Physical Chemistry Chemical Physics* **2013**, *15*, 1976–1989.

(72) Pluhackova, K.; Kirsch, S. A.; Han, J.; Sun, L.; Jiang, Z.; Unruh, T.; Böckmann, R. A. A Critical Comparison of Biomembrane Force Fields: Structure and Dynamics of Model DMPC, POPC, and POPE Bilayers. *Journal of Physical Chemistry B* **2016**, *120*, 3888–3903.

(73) Pandit, K. R.; Klauda, J. B. Membrane models of E. coli containing cyclic moieties in the aliphatic lipid chain. *Biochimica et Biophysica Acta - Biomembranes* **2012**, *1818*, 1205–1210.

(74) Dimova, R. Recent developments in the field of bending rigidity measurements on membranes. *Advances in Colloid and Interface Science* **2014**, *208*.

(75) Dies, H.; Cheung, B.; Tang, J.; Rheinstädter, M. C. The organization of melatonin in lipid membranes. *Biochimica et Biophysica Acta - Biomembranes* **2015**, *1848*, 1032–1040.

(76) Ben-Zichri, S.; Kolusheva, S.; Danilenko, M.; Ossikbayeva, S.; Stabbert, W. J.; Poggio, J. L.; Stein, D. E.; Orynbayeva, Z.; Jelinek, R. Cardiolipin mediates curcumin

interactions with mitochondrial membranes. *Biochimica et Biophysica Acta - Biomembranes* **2019**, *1861*, 75–82.

(77) Alves, A. C.; Ribeiro, D.; Horta, M.; Lima, J. L.; Nunes, C.; Reis, S. A biophysical approach to daunorubicin interaction with model membranes: Relevance for the drug's biological activity. *Journal of the Royal Society Interface* **2017**, *14*.

(78) Petit, P. X.; Lecoeur, H.; Zorn, s. E.; Dauguet, C.; Mignotte, B.; Gougeon, M.-L. Alterations in Mitochondrial Structure and Function Are Early Events of Dexamethasone-induced Thymocyte Apoptosis. *Journal of Cell Biology* **1995**, *130*.

(79) Ma, D.; Pignanelli, C.; Tarade, D.; Gilbert, T.; Noel, M.; Mansour, F.; Adams, S.; Dowhayko, A.; Stokes, K.; Vshyvenko, S.; Hudlicky, T.; McNulty, J.; Pandey, S. Cancer Cell Mitochondria Targeting by Pancratistatin Analogs is Dependent on Functional Complex II and III. *Scientific Reports* **2017**, *7*, 1–21.

(80) Kelley, E. G.; Butler, P. D.; Ashkar, R.; Bradbury, R.; Nagao, M. Scaling relationships for the elastic moduli and viscosity of mixed lipid membranes. *Proceedings of the National Academy of Sciences* **2020**, *117*, 23365–23373.

(81) E, E.; W, R. Entropy-driven tension and bending elasticity in condensed-fluid membranes. *Physical review letters* **1990**, *64*, 2094–2097.

(82) Chen, Q.; Lesnefsky, E. J. Depletion of cardiolipin and cytochrome c during ischemia increases hydrogen peroxide production from the electron transport chain. *Free Radical Biology and Medicine* **2006**, *40*, 976–982.

(83) Ellis, C. E.; Murphy, E. J.; Mitchell, D. C.; Golovko, M. Y.; Scaglia, F.; Barceló-Coblijn, G. C.; Nussbaum, R. L. Mitochondrial Lipid Abnormality and Electron Transport Chain Impairment in Mice Lacking α-Synuclein. *Molecular and Cellular Biology* **2005**, *25*, 10190–10201.

(84) Kiebish, M. A.; Han, X.; Cheng, H.; Chuang, J. H.; Seyfried, T. N. Cardiolipin and electron transport chain abnormalities in mouse brain tumor mitochondria: Lipidomic evidence supporting the Warburg theory of cancer. *Journal of Lipid Research* **2008**, *49*, 2545–2556.

(85) Liberman, E. A.; Topaly, V. P.; Tsofina, L. M.; Jasaitis, A. A.; Skulachev, V. P. Mechanism of coupling of oxidative phosphorylation and the membrane potential of mitochondria. *Nature* **1969**, *222*, 1076–1078.

(86) Chaban, Y.; Boekema, E. J.; Dudkina, N. V. Structures of mitochondrial oxidative phosphorylation supercomplexes and mechanisms for their stabilisation. *Biochimica et Biophysica Acta - Bioenergetics* **2014**, *1837*, 418–426.

(87) Nuñez, G.; Benedict, M. A.; Hu, Y.; Inohara, N. Caspases: The proteases of the apoptotic pathway. *Oncogene* **1998**, *17*, 3237–3245.

(88) Shidoji, Y.; Hayashi, K.; Komura, S.; Ohishi, N.; Yagi, K. Loss of molecular interaction between cytochrome c and cardiolipin due to lipid peroxidation. *Biochemical and Biophysical Research Communications* **1999**, *264*, 343–347.

(89) Rytomaa, M.; Kinnunen, P. K. Reversibility of the binding of cytochrome c to liposomes. Implications for lipid-protein interactions. *Journal of Biological Chemistry* **1995**, *270*, 3197–3202.

(90) Hauser, H.; Pascher, I.; Sundell, S. Preferred Conformation and Dynamics of the Glycerol Backbone in Phospholipids: An NMR and X-ray Single-Crystal Analysis. *Biochemistry* **1988**, *27*, 9166–9174.

(91) Pachence, J. M.; Blasie, J. K. Structural investigation of the covalent and electrostatic binding of yeast cytochrome c to the surface of various ultrathin lipid multilayers using x-ray diffraction. *Biophysical Journal* **1991**, *59*, 894–900.

(92) Kinnunen, P. K.; Kõiv, A.; Lehtonen, J. Y.; Rytömaa, M.; Mustonen, P. Lipid dynamics and peripheral interactions of proteins with membrane surfaces. *Chemistry and Physics of Lipids* **1994**, *73*, 181–207.

(93) Tan, Y.; Zhu, Y.; Zhao, Y.; Wen, L.; Meng, T.; Liu, X.; Yang, X.; Dai, S.; Yuan, H.; Hu, F. Mitochondrial alkaline pH-responsive drug release mediated by Celastrol loaded glycolipid-like micelles for cancer therapy. *Biomaterials* **2018**, *154*, 169–181.

(94) Rytomaa, M.; Mustonen, P.; Kinnunen, P. K. Reversible, nonionic, and pH-dependent association of cytochrome c with cardiolipin-phosphatidylcholine liposomes. *Journal of Biological Chemistry* **1992**, *267*, 22243–22248.

(95) Lenaz, G. Lipid fluidity and membrane protein dynamics. *Bioscience Reports* **1987**, *7*, 823–837.

(96) Rohlena, J.; Dong, L.-f.; Neuzil, J. Targeting the Mitochondrial Electron Transport Chain Complexes for the Induction of Apoptosis and Cancer Treatment. *Current Pharmaceutical Biotechnology* **2013**, *14*.

(97) Fowler, P. W.; Hélie, J.; Duncan, A.; Chavent, M.; Koldsø, H.; Sansom, M. S. Membrane stiffness is modified by integral membrane proteins. *Soft Matter* **2016**, *12*, 7792–7803.

(98) Krauss, S. *Encyclopedia of Life Sciences*; John Wiley & Sons, Ltd, 2001.

(99) Hackenbrock, C. R.; Chazotte, B.; Shaila Gupte, S. The Random Collision Model and a Critical Assessment of Diffusion and Collision in Mitochondrial Electron Transport. *Journal of Bioenergetics and Biomembranes* **1986**, *18*.

(100) VAUHKONEN, M.; SASSAROLI, M.; SOMERHARJU, P.; EISINGER, J. Lateral diffusion of phospholipids in the lipid surface of human low-density lipoprotein mea-

sured with a pyrenyl phospholipid probe. *European Journal of Biochemistry* **1989**, *186*, 465–471.

(101) Reister, E.; Seifert, U. Lateral diffusion of a protein on a fluctuating membrane. *Europhysics Letters* **2005**, *71*, 859–865.

(102) Birk, A. V.; Chao, W. M.; Bracken, C.; Warren, J. D.; Szeto, H. H. Targeting mitochondrial cardiolipin and the cytochrome c/cardiolipin complex to promote electron transport and optimize mitochondrial ATP synthesis. *British Journal of Pharmacology* **2014**, *171*, 2017–2028.

(103) Kalpage, H. A. et al. Cytochrome c phosphorylation: Control of mitochondrial electron transport chain flux and apoptosis. *International Journal of Biochemistry and Cell Biology* **2020**, *121*.

Acknowledgements

The authors would like to thank Dr. Siyaram Pandey for fruitful discussion. This work acknowledges support from: the Natural the Natural Sciences and Engineering Research Council (NSERC) of Canada (funding reference number RGPIN-2018-04841) (D.M.); the Ontario Graduate Scholarship (OGS) program (M.DiP., M.H.L.N., and B.W.R.). B.K. thanks International Max Planck Research School (IMPRS) on Multi-scale Modelling for the funding. M.D. is supported by the National Institute of General Medical Sciences of the NIH under Award Number F32GM134704. Access to the Neutron Spin Echo Spectrometer and NGB30 SANS Instrument was provided by the Center for High Resolution Neutron Scattering, a partnership between NIST and the NSF under Agreement No. DMR-2010792. The identification of commercial products of trade names does not imply endorsement or recommendation by the National Institute of Standards and Technology. This research used resources of the Advanced Photon Source, a U.S. Department of Energy (DOE) Office of

Science User Facility operated for the DOE Office of Science by Argonne National Laboratory under Contract No. DEAC02-06CH11357. The authors thank Dr. Xiaobing Zuo for his help at APS.

Author contributions statement

B.W.R. and D.M. designed the research. S.C., B.W.R., M.H.L.N., M.DiP., and D.M. carried out experimentation and analyzed the data. E.G.K. and M.N. provided expert NSE and SANS help and assisted with data acquisition and analysis. M.D., B.K., A.L.-L., and M.S.M., provided expert MD help and assisted with data acquisition and analysis. S.C. and D.M. wrote the article. All authors reviewed the manuscript.

Supporting Information Available

Supplementary information is available at:

Tables available for: Structural parameters derived from small angle neutron scattering and MD simulations, vesicle composition and mole percent of PST present in various LUV compositions, vesicle size and diffusion coefficient measured by DLS, and structural parameters measured by NSE and MD simulations.

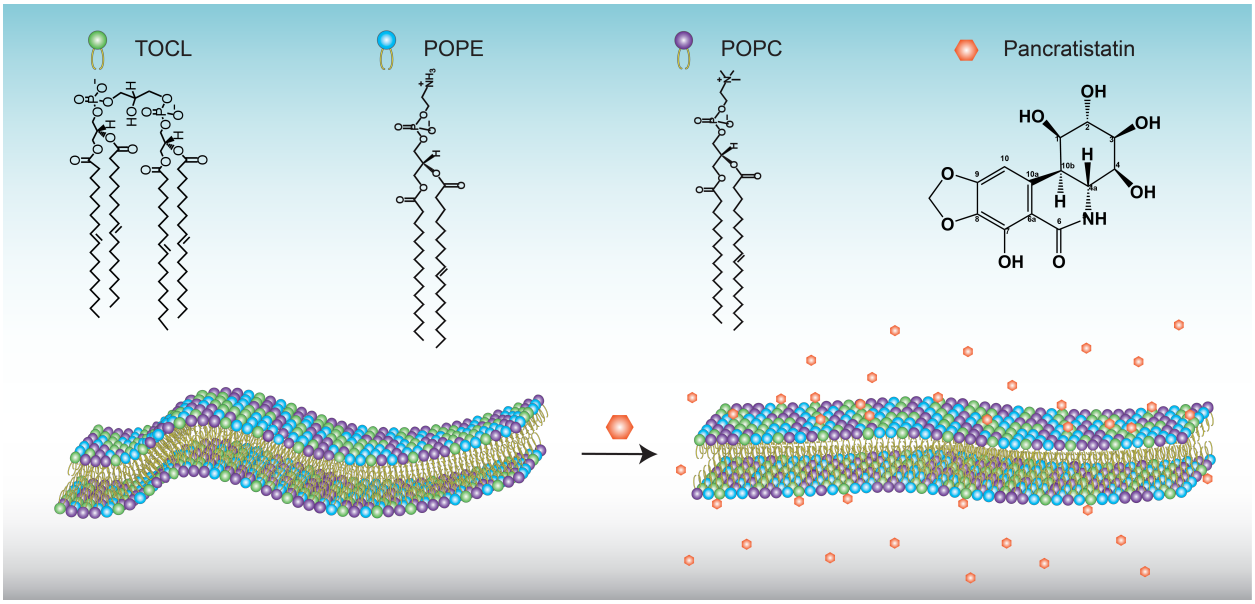

Graphical Abstract

TOC Graphic